Simulations of a micro-PET system based on liquid xenon

2012 Phys. Med. Biol. 57 1685

(http://iopscience.iop.org/0031-9155/57/6/1685)

IOP Publishing Physics in Medicine and Biology

Phys. Med. Biol. **57** (2012) 1685–1700 doi:10.1088/0031-9155/57/6/1685

Simulations of a micro-PET system based on liquid xenon

A Miceli[1], J Glister[1], A Andreyev[2], D Bryman[2], L Kurchaninov[1], P Lu[1], A Muennich[1], F Retiere[1] and V Sossi[2]

[1] TRIUMF, 4004 Wesbrook Mall, Vancouver V6T 2A3, Canada
[2] Department of Physics and Astronomy, University of British Columbia, 6224 Agricultural Road, Vancouver V6T 1Z1, Canada

Received 12 July 2011, in final form 4 January 2012
Published 7 March 2012
Online at stacks.iop.org/PMB/57/1685

Abstract

The imaging performance of a high-resolution preclinical micro-positron emission tomography (micro-PET) system employing liquid xenon (LXe) as the gamma-ray detection medium was simulated. The arrangement comprises a ring of detectors consisting of trapezoidal LXe time projection ionization chambers and two arrays of large area avalanche photodiodes for the measurement of ionization charge and scintillation light. A key feature of the LXePET system is the ability to identify individual photon interactions with high energy resolution and high spatial resolution in three dimensions and determine the correct interaction sequence using Compton reconstruction algorithms. The simulated LXePET imaging performance was evaluated by computing the noise equivalent count rate, the sensitivity and point spread function for a point source according to the NEMA-NU4 standard. The image quality was studied with a micro-Derenzo phantom. Results of these simulation studies included noise equivalent count rate peaking at 1326 kcps at 188 MBq (705 kcps at 184 MBq) for an energy window of 450–600 keV and a coincidence window of 1 ns for mouse (rat) phantoms. The absolute sensitivity at the center of the field of view was 12.6%. Radial, tangential and axial resolutions of ^{22}Na point sources reconstructed with a list-mode maximum likelihood expectation maximization algorithm were $\leqslant$0.8 mm (full-width at half-maximum) throughout the field of view. Hot-rod inserts of $<$0.8 mm diameter were resolvable in the transaxial image of a micro-Derenzo phantom. The simulations show that a LXe system would provide new capabilities for significantly enhancing PET images.

(Some figures may appear in colour only in the online journal)

1. Introduction

Positron emission tomography (PET) is a functional medical imaging technique of increasing importance. Its power resides in the ability to investigate biological processes that are altered by disease and to trace radio-labeled molecules in organs. PET imaging can be used for early cancer screening, studying the pathology of illness and to guide the development of new drugs.

Table 1. Properties of LXe .

Property	Value
Atomic number	54
Density	3.1 g cm^3
Boiling point	$T = 165$ K at 1 atm
Melting point	$T = 161$ K at 1 atm
Photofraction at 511 keV	22%
Attenuation length at 511 keV	37 mm
Decay time	2.2 ns, 27 ns

Recently, several efforts were made to improve the sensitivity and spatial resolution of preclinical PET scanners by developing scintillation crystal-based detectors capable of measuring depth of interaction (DOI) (Roldan *et al* 2007, Seidel *et al* 2002, Yang *et al* 2008).

We are developing a novel high-resolution preclinical PET system using ionization and scintillation light signals from gamma-ray interactions in liquid xenon (LXe). The time projection chamber (TPC) (Marx *et al* 1978) configuration is employed where ionization electrons are collected without the gain of electrodes after drifting 11 cm under an applied electric field of 1–3 kV cm^{-1}. Ionization from photon interactions can be localized in 3D to <1 mm because electron diffusion is small in LXe. Low diffusion also allows the separation of individual photon interactions. Charge collection efficiency is high as long as the level of impurities in the LXe is sufficiently low (ppb level) (Chepel *et al* 1994, Conti *et al* 2003). Photon interactions also produce copious scintillation light in LXe (68 000 photons MeV^{-1} at zero electric field) with time constants of 2.2 and 27 ns, which is detected in our set-up by a set of large area avalanche photo-diodes (LAAPD) (Moszynski *et al* 2002); scintillation light is used to measure the interaction time with high resolution and contributes to the energy measurement. Furthermore, using both charge and scintillation light, excellent energy resolution (<4% FWHM at 662 keV) has been reported (Aprile *et al* 2007). LXe can be used to cover large detection volumes with high uniformity over the entire field of view (FOV) improving the detection sensitivity. Our previous studies on the use of LXe as a detection medium in PET were reported in Amaudruz *et al* (2009). The relevant properties of LXe are listed in table 1.

In this paper, we describe a simulation of a LXe μ-PET scanner and the Compton reconstruction algorithm developed for sequencing multi-interaction events. In addition, we present the simulated imaging performance of the LXePET system including sensitivity, scatter fraction and spatial resolution evaluated according to the National Electrical Manufacturers Association (NEMA) standard NU4 (NEMA 2008) and the image of a micro-Derenzo phantom.

2. Simulation framework

2.1. Simulation model

Figure 1 shows the planned configuration of the LXePET scanner consisting of 12 trapezoidal sectors arranged in a ring geometry. The inner bore has 10 cm diameter and 10 cm axial length. The LXe is contained in a stainless-steel vessel thermally insulated by a vacuum space. Each sector is a LXeTPC viewed by two arrays of LAAPDs. The anode and cathode areas are 10×9.2 cm^2 and 10×3.2 cm^2, respectively, and the drift length is 11.2 cm. Each APD array consists of seven APDs with 16 mm diameter, nine APDs with 10 mm diameter and

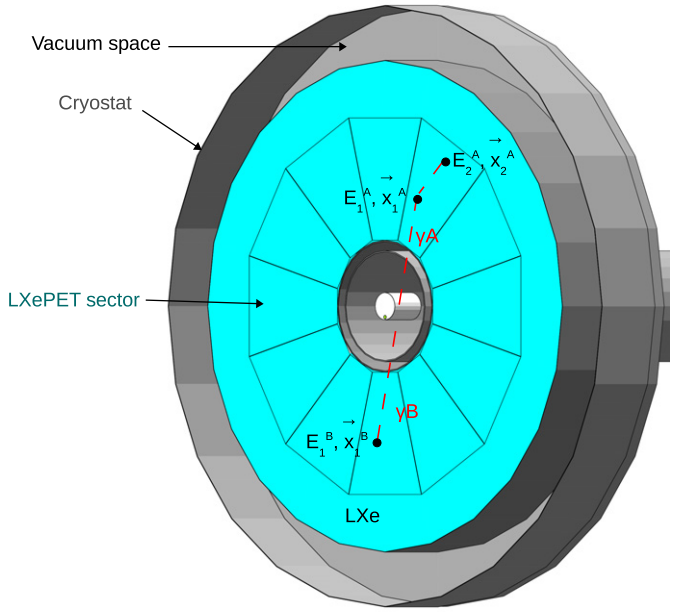

Figure 1. Simulated LXe PET system. The cryostat, the 12 LXePET sectors, the inner vessel filled with LXe, and the mouse-like NEMA phantom are illustrated. The dashed lines indicate a pair of annihilation photons which interact in the LXe. In this figure, photon A interacts twice in the LXePET sector, first via Compton scattering, then via the photoelectric effect. Photon B interacts only once via the photoelectric effect. Energy and 3D position of each photon interaction are recorded by the TPC.

eight APDs with 5 mm diameter. Smaller APDs are used in the inner region to enhance the reconstruction where most of the events occur. Figure 2 shows the APD layout in one of the sectors.

The simulation of the LXe prototype was carried out with the Geant4 simulation package (Agostinelli *et al* 2003). A positron emitter (^{18}F or ^{22}Na depending on the study) was simulated. Following the decay of the radioisotope, positrons with energy sampled from a continuous distribution of the beta decay process were generated and tracked until annihilation. To simulate the non-colinearity of the annihilation photons, a new process was created and integrated in Geant4. The new process simulates the positron annihilation in-flight according to the Geant4 annihilation process and replaces the Geant4 annihilation at rest with a model where the non-zero momentum of the electron–positron pair is taken into account. The interactions of the annihilation photons with the phantom and PET scanner were simulated with the low-energy package of Geant4. Energy and 3D position of every photon interaction in the LXe detector were recorded. The numbers of ionization charges N^i_{e-} and scintillation photons S_i created in the interactions were calculated as Miceli *et al* (2011):

$$N^i_{e-} = \frac{(1 - \mathrm{Fr}^*) \times E^{G4}_i}{15.6eV} \tag{1}$$

$$S^i = \frac{(\upsilon + \mathrm{Fr}^*) \times E^{G4}_i}{15.6eV} \tag{2}$$

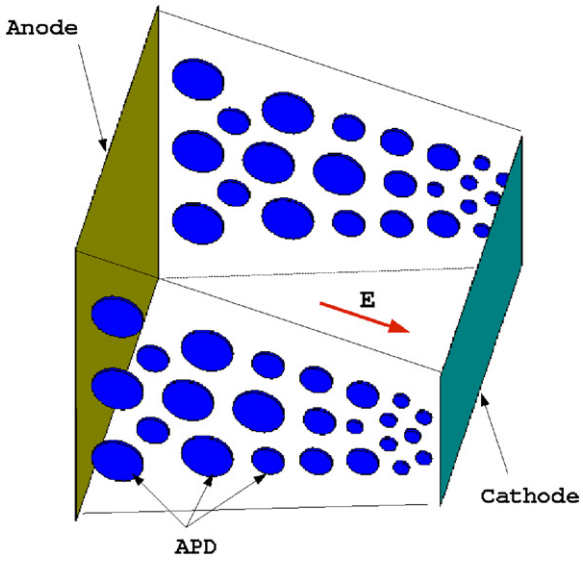

Figure 2. APD layout in one of the LXePET sectors.

Table 2. Simulation parameters.

Quantity	Symbol	Value
Recombination factor	Fr	0.24
Fluctuation of the e–ion recombination	Δ Fr	0.032
Position resolution	σ_{pos}	0.3 mm
Minimum two-hits separation distance	d	1 mm
Electronic noise charge (APD 16 mm)	ENC_A^{16}	5000 e-
Electronic noise charge (APD 10 mm)	ENC_A^{10}	2000 e-
Electronic noise charge (APD 5 mm)	ENC_A^{5}	500 e-
APD quantum efficiency	QE	80%
APD gain	G	500
APD excess noise factor	F	2.5
TPC electronic noise	ENC_Q	600 e-
Charge detection threshold	T_C	1800 e-

where Fr* is the electron–ion recombination fraction, E_i^{G4} is the energy deposited in the interaction i and $\upsilon = 0.2$ (Aprile *et al* 2007) is the ratio of the number of excitons and ion pairs produced. The electron–ion recombination fraction Fr* varies on an event-by-event basis. It was modeled as a Gaussian function centered at $\text{Fr} = 0.24$ with width $\Delta Fr = 0.032$ (Amaudruz *et al* 2009). Electronics and photo-detectors were not simulated directly. Instead, instrumental responses were parameterized in subsequent analyses as described in Miceli *et al* (2011). The parameters used in the simulation are listed in table 2.

2.2. Event selection

Coincidence events were selected using a two-step procedure. The first stage of the event selection simulated the response of the detector trigger using only the information from the scintillation light. Events producing less than 5000 scintillation photons (corresponding to

approximately 180 keV) were rejected. For each photon of each annihilation pair passing the first selection stage, we calculated the energy from the scintillation light corrected for the solid angle using the information of the position from the charge measurement (Miceli *et al* 2011) and we used the resulting value to calculate the light-charge combined energy as described in Aprile *et al* (2007). Events with combined energy 450–600 keV were kept. The first interaction points defining the lines of response (LOR) of the selected events were stored in a list-mode format. The Compton reconstruction algorithm described in section 2.3 was used to find the first interaction point for multi-sites events.

2.3. Compton reconstruction algorithm

When a photon interacts in the detector, it can Compton scatter multiple times before being photo-absorbed. A 511 keV photon is roughly three times more likely to Compton scatter than be photo-absorbed when it first interacts in LXe. The simplest interaction configuration is the 1–1 case in which the detector registers only one discernible interaction point for each of the two photons, corresponding to photo-absorption without scattering. Practically, however, multi-hit scenarios such as 1–2, 1–3, 2–2, etc are more common, and must be taken into account, as they contribute to blurring of the image due to ambiguity in the location of the first interaction point. The goal of the Compton reconstruction algorithm is to sort through all the possible scattering sequences, determine the path that is the most probable, and define the most likely first interaction point and its associated LOR.

For each pair of photons interacting $M - N$ times in the detector, with M representing photon 1 and N photon 2, and $M \leqslant N$, there are $M!N!$ number of possible interaction sequences. For each sequence, a LOR check is first performed, determining whether the trajectory passes through the phantom. Then, if the sequence was found to be viable, Compton kinematics were used to compute a test statistic score associated with the sequence.

The Klein–Nishina formula determines the scattering angle based on the energy deposited:

$$\cos(\theta_E) = 1 + mc^2 \times \left(E_{\gamma i}^{-1} - E_{\gamma i+1}^{-1}\right) \tag{3}$$

where $E_{\gamma i}$ is the photon energy before the ith step given by

$$E_{\gamma i} = E_{\gamma 1} - \sum_{j=1}^{i-1} \mathrm{d}E_j, \tag{4}$$

where m is the electron mass, θ_E is the Compton scattering angle, $\mathrm{d}E_j$ is the energy deposited at the jth step and $E_{\gamma 1} = 511$ keV is the energy of the photon before it reaches the detector. Alternatively, the scattering angle θ_G based on the position of the interaction site is calculated as

$$\cos(\theta_G) = \frac{\vec{u_i} \cdot \vec{u_{i+1}}}{|\vec{u_i}||\vec{u_{i+1}}|}, \tag{5}$$

where $\vec{u_i} = (x_i - x_{i-1}, y_i - y_{i-1}, z_i - z_{i-1})$.

For each candidate interaction site, we could, in principle, determine if the sequence was the correct one by comparing the scattering angles computed using the energy deposited (θ_E) with the observed scattering angles given the geometric distribution of interaction sites (θ_G). In the ideal situation, the difference would be zero.

The ability to resolve the correct sequence, however, depends on the position and energy resolution of the system. A statistical weighting was used to account for instrumental resolution limits:

$$\chi^2 = \sum_{i=1}^{N-1} \frac{(\cos(\theta_E)_i - \cos(\theta_G)_i)^2}{\Delta\cos(\theta_E)_i^2 + \Delta\cos(\theta_G)_i^2}, \tag{6}$$

where the error terms are defined as Aprile *et al* (2008):

$$\Delta\cos(\theta_E)_i^2 = m^2c^4 \times \left(\frac{\sigma_{\mathrm{d}E_i}^2}{E_{\gamma i}^4} + \sigma_{E\gamma i+1}^2 \times \left(E_{\gamma i}^{-2} - E_{\gamma i+1}^{-2}\right)^2\right) \tag{7}$$

and

$$\Delta\cos(\theta_G)_i^2 = \sigma_{\mathrm{pos}}^2 \times (\sigma g_{i,x} + \sigma g_{i,y} + \sigma g_{i,z}), \tag{8}$$

where

$$\sigma\vec{g}_i = \left(\frac{\vec{u_{i+1}}}{|\vec{u_i}|\cdot|\vec{u_{i+1}}|} - \frac{\vec{u_i}\times\cos(\theta_G)}{|\vec{u_i}|^2}\right)^2 + \left(\frac{\vec{u_i}}{|\vec{u_i}|\cdot|\vec{u_{i+1}}|} - \frac{\vec{u_{i+1}}\times\cos(\theta_G)}{|\vec{u_{i+1}}|^2}\right)^2. \tag{9}$$

The error on the energy deposited at the ith step, $\sigma_{\mathrm{d}E_i}$, and the error on the photon energy after the interaction step i, $\sigma_{E\gamma i+1}$, are given by

$$\sigma_{\mathrm{d}E_i}^2 = \mathrm{ENC}_Q^2 + \Delta\,\mathrm{Fr}^2 \times \mathrm{d}E_i^2, \tag{10}$$

$$\sigma_{E\gamma i+1}^2 = \mathrm{i} \times \mathrm{ENC}_Q^2 + \Delta\,\mathrm{Fr}^2 \times \sum_{j=1}^{i} \mathrm{d}E_j^2. \tag{11}$$

Finally, the viable sequence with the lowest test statistic score was chosen by the reconstruction algorithm, and the associated LOR was defined and recorded. If no suitable interaction sequence was found, then the event was discarded. This reconstruction technique is similar to the one used in Oberlack *et al* (2000), Aprile *et al* (2008) modified for PET applications.

2.4. Pile-up

At high rates, fast scintillation light signals are used to roughly (1 cm^3) localize the event in order to match correctly the light signal with the slowly drifting charge. Pile-up of events can occur in the small volume determined by the light localization region and may contribute to the count losses. In order to improve the count rate capability of the LXePET system, a pile-up event recovery method based on energy balance and proximity to the light signal was developed. The efficiency of the algorithm was found to be 99%, 95% and 89% for two, three and four events, respectively, of simulated pile-up. The fraction of pile-up events was evaluated by simulating a mouse and a rat phantom filled with water and ^{18}F. The time of each decay was simulated using a Poisson distribution. The count rate correction factor for the pile-up with the recovery method, ϵ_p, is given by

$$\epsilon_p = f_s + \sum_{k=2}^{4} f_e^k \times \mu^k, \tag{12}$$

where f_s is the fraction of pile-up free events, f_e^k is the fraction of k-events pile-up and μ^k is the efficiency of the pile-up recovery method for k-events pile-up.

2.5. Detection rate calculation

The output of the simulation consisted of interaction steps for two types of events: singles where only one of the two photons interacted with the detector and double events where both photons reached the detector. These data are source activity independent and do not contain random coincidence events. In order to simulate the count rate performance of the LXe detector, the detection rates at different source activities and instrumental parameters, such as dead time and coincidence window, had to be calculated. Also, count losses due to the pile-up of events in the TPC were taken into account.

Table 3. Trigger probabilities for zero, one, two photons (P_0, P_1, P_2), and probabilities (ϵ_2, ϵ_{2r}) of a triggered event to pass the event selection for non-random and random events.

		Mouse-like phantom	Rat-like phantom
Scenario	$[P_0]$ (%)	41.5	40.8
	$[P_1]$ (%)	36.3	46.6
	$[P_2]$ (%)	22.2	12.6
Efficiency	ϵ_2 (%)	43.3	33.5
	ϵ_{2r} (%)	3.39	6.26

The calculation of detection rates was done by Poisson statistical modeling, taking into account the probability of each interaction type, and assuming that only events with exactly two emitted photons detected were selected. Given the trigger probabilities of detecting zero (P_0), one (P_1), and two (P_2) photons from annihilation, the trigger rates for true and scatter events $C_{2,0}$ and for random events $C_{2r,0}$ for a given source activity, A, and coincidence window, Δt, can be computed:

$$C_{2,0}(A) = \frac{1}{\Delta t}\sum_{k=1}^{\infty}\frac{\mathrm{e}^{-\lambda}\lambda^k}{k!}P_2P_0^{k-1}, \qquad \text{where} \quad \lambda = A * \Delta t \tag{13}$$

and

$$C_{2r,0}(A) = \frac{1}{\Delta t}\sum_{k=2}^{\infty}\frac{\mathrm{e}^{-\lambda}\lambda^k}{k!}P_1^2P_0^{k-2}. \tag{14}$$

Coincidence windows of 1, 3 and 6 ns were considered in these studies. The count rate for true and scatter events $C_2(A)$ and for randoms $C_{2r}(A)$ are calculated as

$$C_2(A) = \frac{C_{2,0}}{1 + C_{\text{total},0}\tau}\epsilon_2 \times \epsilon_p^2, \tag{15}$$

$$C_{2r}(A) = \frac{C_{2r,0}}{1 + C_{\text{total},0}\tau}\epsilon_{2r} \times \epsilon_p^2, \tag{16}$$

where τ is the instrumental dead time, ϵ_p is the count rate correction factor for the pile-up (equation 12), and ϵ_2 and ϵ_{2r} are the probabilities of a triggered event to pass the event selection criteria. $C_{\text{total},0}$ is the total trigger rate including random coincidences. The ratios ϵ_2 and ϵ_{2r} depend on the combined energy resolution and energy window threshold, as well as on the event reconstruction strategy used. They are calculated for each data set (simulated true plus scatter data set and random data set) as the number of events which have combined energy within the 450–600 keV energy window and define a LOR which passes through the phantom, divided by the number of triggered events. The random set was generated by combining single unrelated events in pairs. The first-stage trigger probabilities for zero, one, two photons detection, and second-stage event selection efficiencies are given in table 3. The trigger probability of detecting one or two photons is 60% for both the mouse and rat phantoms. The probability of detecting two photons depositing more than 180 keV is 22%, significantly higher for the mouse phantom than 13% found for the rat phantom due to the smaller amount of scattering produced by the mouse phantom. The amount of scattering is related to the size of the phantom.

Once the two final detection rates were calculated, a rate dependence could be applied to the output of the Geant4 simulation. This was done by scaling the simulated double (true and scatter) and random events (pair-wise combinations of single events) to obtain

the total detection rate $C_2(A) + C_{2r}(A)$. This scaling approach allowed us to use a single large set of simulation data to compute the behavior of the detector and its performance at various resolution limits and activities without the need to re-simulate under different detector parameters.

2.6. Image reconstruction

In order to preserve the high-resolution spatial information contained in the data produced by the LXePET scanner, we reconstructed the point source data and the micro-Derenzo phantom with a list-mode reconstruction algorithm. The main advantages of list-mode data reconstruction over rebinned data reconstruction are preservation of the maximum sampling frequency, and faster reconstruction for low-statistics frames. Data reconstructed with histogram-mode methods are compressed in the axial and radial directions to reduce the sinogram size and to accelerate the reconstruction with a consequent loss of axial and transaxial resolution (Arman *et al* 2005). This effect is particularly evident moving away from the axial axis in the transaxial plane. List-mode methods reconstruct the data event by event without the need of binning the data into space and time intervals thereby preventing information losses. The information preserving characteristic of list-mode reconstruction methods is particularly useful for high spatial and temporal resolution PET systems (Reader *et al* 2004). The computational time of histogram-mode reconstruction methods depends on the number of LOR in the sinogram, whereas reconstruction time of list-mode methods depends only on number of events recorded. List-mode methods are therefore preferred for high-resolution scanners where the number of LOR can be much higher than the number of recorded events (Arman *et al* 2005). List-mode image reconstruction methods are also favorable in time-of-flight PET (Pratx *et al* 2011), motion corrected PET (Lamare *et al* 2007) and dynamic and gated PET (Rahmim *et al* 2005). We used a 3D list-mode image reconstruction algorithm for PET based on the maximum likelihood expectation maximization (MLEM) approach (Shepp and Vardi 1982). As in Barrett *et al* (1997) and Parra and Barrett (1998) each detected LOR was considered as a unique projection bin with the number of counts in each projection bin g_i equal to 1. Using notations f_j^n and f_j^{n+1} for the intensity vectors in voxel j for step n and the next $n+1$ iteration estimates, the iteration step for the list-mode MLEM algorithm is equal to

$$f_j^{n+1} = \frac{f_j^n}{s_j} \sum_i p_{ji} \frac{1}{\sum_k p_{ik} f_k^n}, \tag{17}$$

where p_{ij} is the value of the system matrix describing the probability that a given emission event i originates from a certain voxel j and s_j is the sensitivity value for voxel j. The list-mode MLEM used *on-the-fly* ray-driven forward and back projection with bilinear interpolation (Rahmim *et al* 2004). We used 20 MLEM iterations for the ^{22}Na point sources and 100 MLEM iterations for the Derenzo phantom. The voxel size was $0.15 \times 0.15 \times 0.15$ mm^3 and the image size was $360 \times 360 \times 360$ voxels. The reconstruction time for point sources (5.5 million LORs on average) was less than 3 h on an Intel Xeon 2.00 GHz CPU (single core). The reconstruction speed of the list-mode MLEM algorithm can be further improved by using the ordered subsets approach (Hudson and Larkin 1994) and parallel processing.

2.7. Simulated data

The system performance was evaluated based on the NEMA standards (NEMA 2008). The only deviation from the NEMA protocol was the use of a list-mode MLEM reconstruction method instead of FBP reconstruction algorithm for the spatial resolution studies. As explained

in section 2.6, we used the list-mode MLEM method in order to preserve the high-resolution spatial information of the scanner.

Sensitivity. The sensitivity of the system was determined with a Na^{22} point source embedded in a 1 cm^3 acrylic cube. The source was stepped axially over the axial length of the scanner. The data were rebinned using the SSRB.

Scatter fraction and count rate performance. The scatter fraction and count rate performance were obtained with a mouse- and a rat-like phantoms. The mouse-like phantom was a 25 mm diameter and 70 mm length polyethylene cylinder with a 3.2 mm diameter hole drilled at a radial distance of 10 mm. A simulated 3.2 mm diameter and 60 mm long rod was filled with water and ^{18}F. The rat-like phantom was a 50 mm diameter and 150 mm length polyethylene cylinder with a 3.2 mm diameter hole drilled at a radial distance of 17.5 mm. A simulated 3.2 mm diameter and 140 mm long rod was filled with water and the ^{18}F. The data were rebinned using the SSRB.

Spatial resolution. The spatial resolution was obtained with the Na^{22} point source used for the sensitivity studies. The source was placed at two axial positions 0 and 12.5 mm and five radial positions 0, 5, 10, 15 and 25 mm. The simulated data were reconstructed with the list-mode MLEM iterative method.

Image quality: The image quality was studied with a micro-Derenzo phantom made from acrylic measuring 40 mm in diameter and 35 mm in length. Arrayed throughout the phantom were cylindrical rods of length 30 mm and diameters 1.6, 1.4, 1.2, 1.0, 0.8 and 0.6 mm. The rods were offset radially by 7 mm from the phantom center and filled with water and ^{18}F. The rod-to-rod separation was set to twice the rod diameter. The simulated data were reconstructed with the list-mode MLEM iterative method.

3. Analysis

3.1. Sensitivity

The absolute sensitivity was calculated following the NEMA standard. A simulated ^{22}Na point source was used for this study. The point source was stepped axially through the scanner at 0.5 mm steps over an axial length of 100 mm. One million ^{22}Na decays were simulated at each step. The total absolute sensitivity for mouse applications was calculated by summing the sensitivity for the sinograms which encompass the central 7 cm. Since the axial extent of the scanner was less than the length of the rat phantom, we calculated the total absolute sensitivity for rat applications summing all the slices, as described in the NEMA standard. The absolute sensitivity at the center of the FOV (CFOV) for an energy window of [450 ,600] keV was 12.6 %. The sensitivity profile for all axial steps can be seen in figure 3. The total absolute sensitivity for mouse and rat applications were 9.4% and 7.2%. The total system sensitivity was 7.2%. For comparison, typical values of the absolute sensitivity at CFOV range from 3.4% for the micro-PET FOCUS-220 with 7.6 cm axial FOV, 250–750 keV energy window and 10 ns time window (Tai *et al* 2005) to 9.3% for the inveon system with 12.7 cm axial FOV, 250–625 keV energy window and 3.4 ns time window (Bao *et al* 2009).

3.2. Scatter fraction and count rate performance

The scatter fraction and noise equivalent count rate (NECR) studies were carried out using the rat- and mouse-like phantoms following the NEMA protocol. For each phantom 50 million

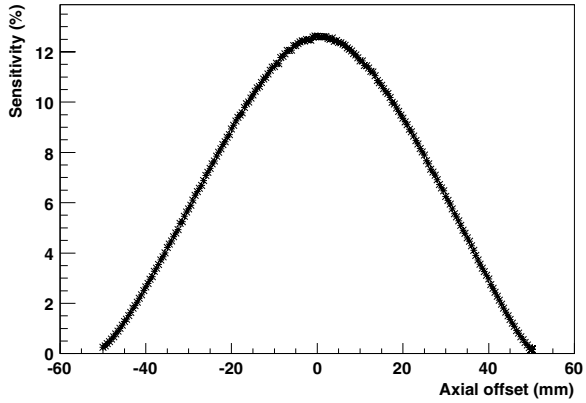

Figure 3. NEMA standard sensitivity profile for a ^{22}Na point source embedded in a 1 cm^3 acrylic cube, measured at 0.5 mm axial steps. Energy window: [450, 600] keV.

^{18}F decays were simulated. The list-mode simulated true plus scatter data set was arranged in sinograms (radial bin size 0.3 mm) and oblique slices were combined into 2D projections using the SSRB method with a 1 cm slice thickness. For each sinogram, all pixels located farther than 8 mm from the edges of the phantom were set to zero. The profile of each projection angle was shifted so that the maximum value was aligned with the central pixel of the sinogram. All the angular projections were then summed to generate a sum projection. All counts outside the central 14 mm band were assumed to be scatter counts. To evaluate the scatter inside the 14 mm central band, we used a linear interpolation. For each slice i, the number of scatter counts $C_{\text{scatt},i}$ was given by the total scatter counts in the sinogram (outside and inside the central 14 mm band) divided by the number of pairs in the data set. The total event count $C_{\text{TOT},i}$ is the sum of the pixels in the projections divided by the number of pairs in the data set. The scatter fraction is given by

$$\text{SF} = \sum_{i=1}^{\text{NSlices}} C_{\text{scatt},i}/C_{\text{TOT},i}. \tag{18}$$

The mouse (rat) scatter fraction was 12.1% (20.8%), of which 4.9% (10.5%) was due to scatter only and 7.2% (10.3%) was due to ambiguities in the Compton reconstruction algorithm. A future paper will deal with reducing the ambiguities. An example of Compton ambiguity involves multi-interaction events where one or both photons interact in only two locations and deposit the same amount of energy. To calculate the percentage of the scatter fraction due to Compton ambiguities, we selected only true events in the simulation data set.

The random set was arranged in sinograms (radial bin size 0.3 mm) and oblique slices were combined into 2D projections using the SSRB method with a 1 cm slice thickness. The number of random counts $C_{\text{random},i}$ for each slice was the total counts in the random coincidence sinogram within 8 mm from the edges of the phantom divided by the number of pairs in the random set.

The noise equivalent rate for each slice was calculated as follows, where $C_2(A)$ and $C_{2r}(A)$ are the rates previously calculated:

$$\text{NECR}_i(A) = \sum_{i=1}^{\text{NSlices}} \frac{((C_{\text{TOT},i} - C_{\text{scatt},i}) \times C_2(A))^2}{C_{\text{TOT},i} \times C_2(A) + C_{\text{random},i} \times C_{2r}(A)} \tag{19}$$

The NECR curves for mouse and rat phantoms are plotted in figure 4 for 1, 3 and 6 ns coincidence windows. The scatter fractions (SF), peak true counting rate ($R_{t,\text{peak}}$), peak

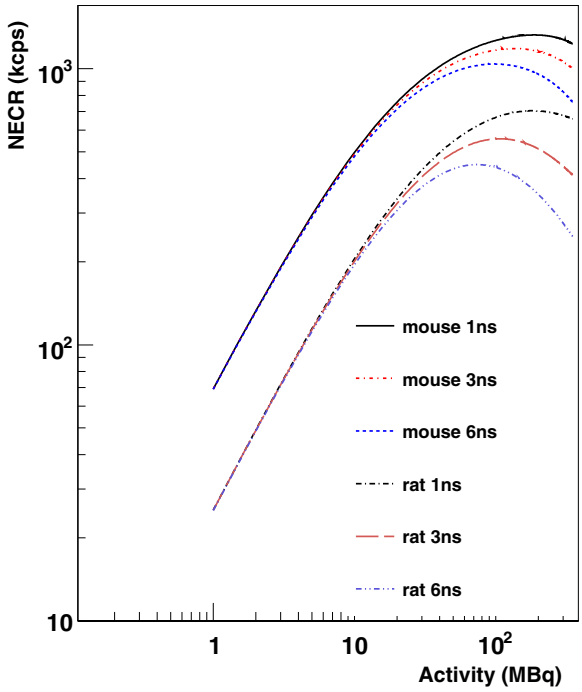

Figure 4. NECR versus total activity, for mouse and rat phantoms and coincidence windows of 1, 3 and 6 ns. The dead time was 0.2 μs and the energy window was [450, 600] keV.

Table 4. Scatter fraction and count rate performance for rat and mouse phantoms. The dead time was 0.2 μs and the energy window was [450, 600] keV.

Phantom	Coincidence Window (ns)	SF (%)	$R_{t,\mathrm{peak}}$ (kcounts)	$R_{\mathrm{NEC,peak}}$ (kcounts)	$A_{t,\mathrm{peak}}$ (MBq)	$A_{\mathrm{NEC,peak}}$ (MBq)
Rat	1	20.8	909	705	202	184
	3		736	558	122	108
	6		605	450	86	75
Mouse	1	12.1	1515	1326	191	188
	3		1359	1183	141	136
	6		1200	1041	103	99

noise equivalent count rate ($R_{\mathrm{NEC,peak}}$), activity at which $R_{t,\mathrm{peak}}$ is reached, and activity at which $R_{\mathrm{NEC,peak}}$ is reached can be found in table 4 for mouse and rat phantoms and the three coincidence windows with an energy window of [450 600] keV. Figure 5 shows true, scatter, random, total counts and NECR as a function of activity for the mouse-like phantom with coincidence window 6 ns and dead time 0.2 μs. The simulated results show a similar usable range of activity compared with commercial micro-PET systems (1670 kcps at 130 MBq for a mouse phantom, a 350–625 keV energy window and 3.4 ns timing window—Inveon (Bao *et al* 2009)).

3.3. Spatial resolution

Spatial resolution was determined using the ^{22}Na point source with diameter 0.25 mm embedded in a 1 cm^3 acrylic cube. A total of 50 million ^{22}Na decays were simulated and an energy window of [450, 600] keV was used. It was assumed that the source activity would

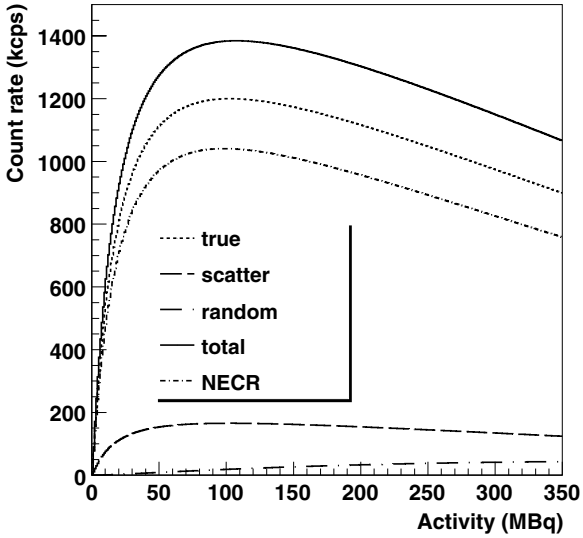

Figure 5. True, scatter, random, total counts and NECR versus total activity, for a mouse-like phantom and coincidence window 6 ns. The dead time was 0.2 μs and the energy window was [450 ,600] keV.

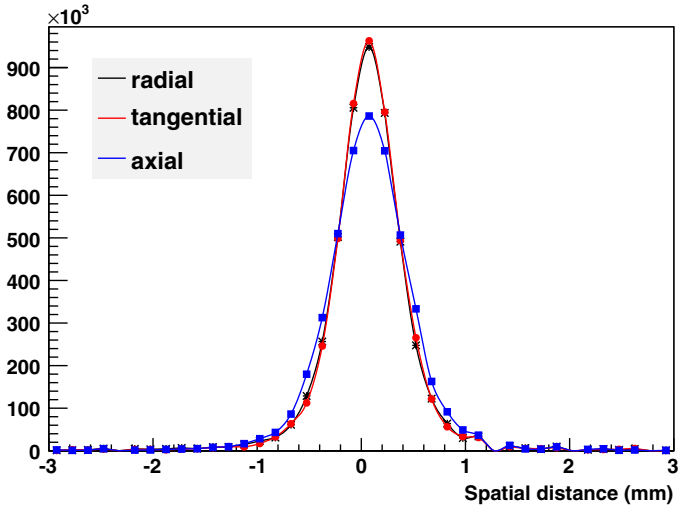

Figure 6. Point spread function in radial, tangential and axial directions of a ^{22}Na point source at CFOV reconstructed with list-mode MLEM. Radial, tangential and axial resolutions (FWHM) were 0.6, 0.6 and 0.8 mm, respectively.

be low enough that random coincidences could be ignored. The source was placed at two axial positions: 0 and 12.5 mm. Five radial positions were used for each axial position: 0, 5, 10, 15 and 25 mm. The data were reconstructed with the list-mode MLEM iterative method (voxel size 0.15 × 0.15 × 0.15 mm^3, 20 iterations). The point spread functions were formed by summing one-dimensional profiles parallel to the direction of measurement and within two FWHM of the orthogonal directions. The FWHM and FWTM values were calculated through

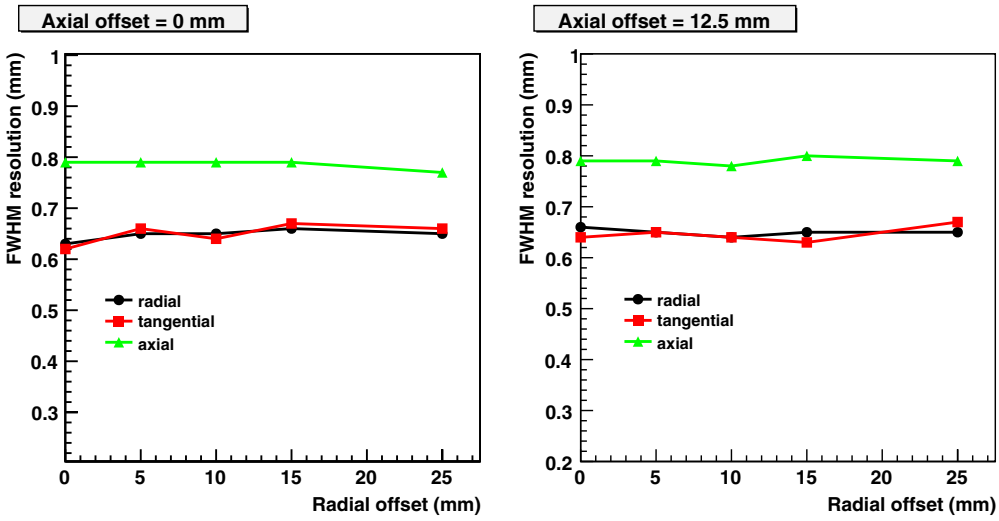

Figure 7. Radial, tangential, and axial resolution (FWHM) of a ^{22}Na point source reconstructed with list-mode MLEM.

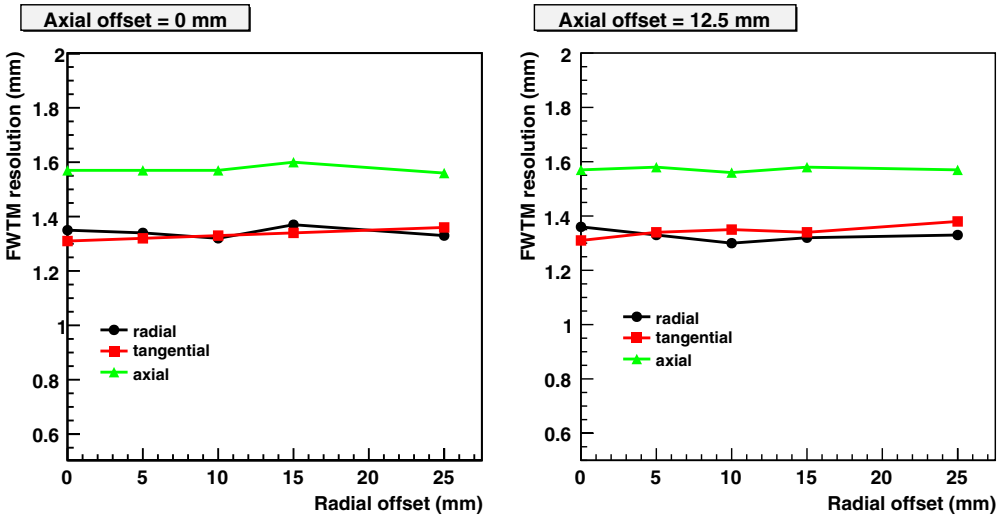

Figure 8. Radial, tangential and axial FWTM of a ^{22}Na point source reconstructed with list-mode MLEM.

linear interpolation between adjacent pixels at one-half and one-tenth of the peak value in each direction. The point spread function for a point source at the CFOV is shown in figure 6.

Radial, tangential and axial resolutions, reported as FWHM and FWTM, are given in figures 7–8. At the CFOV radial, tangential and axial FWHM resolutions of 0.6, 0.6 and 0.8 mm, respectively, were found. At 25 mm radial and 12.5 mm axial offset, radial, tangential and axial FWHM resolutions were 0.7, 0.7 and 0.8 mm, respectively. The results show a uniform resolution $\leqslant$ 0.8 mm (FWHM) throughout the FOV in radial, tangential and axial directions. At the CFOV, the 2D FBP gave the same results of the MLEM algorithm. For comparison, typical values of spatial resolution for conventional micro-PET systems are 1.3,

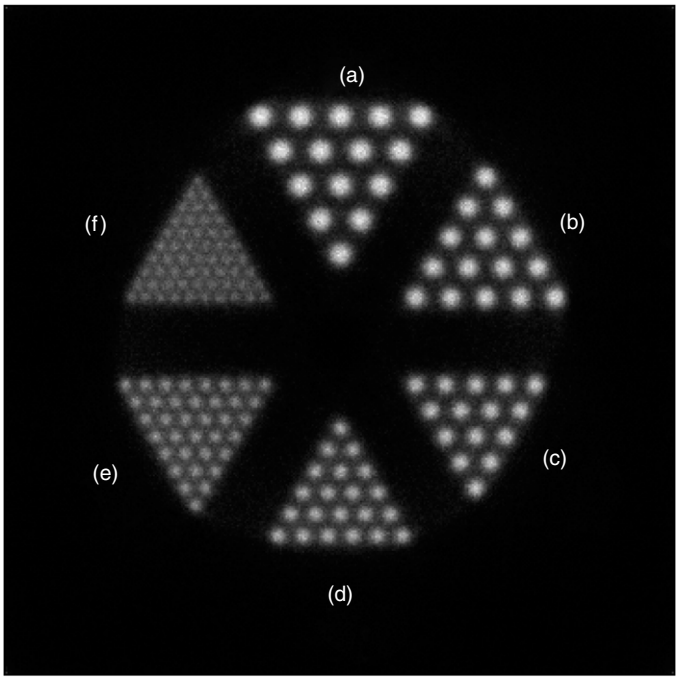

Figure 9. Micro-Derenzo phantom reconstructed using MLEM. Rod-to-rod separation is twice the rod diameter. Rod diameters: (a) 1.6 mm, (b) 1.4 mm, (c) 1.2 mm, (d) 1.0 mm, (e) 0.8 mm and (f) 0.6 mm.

1.3 and 1.5 mm (micro-PET FOCUS-220 (Tai *et al* 2005)). Also, the deterioration of the radial resolution towards the periphery of the FOV, which is common for crystal-based preclinical PET systems due to lack of DOI information, is absent in the LXePET.

3.4. Micro–Derenzo phantom study

Figure 9 shows a trans-axial slice (thickness 24 mm) of the micro-Derenzo phantom with cylindrical rods of length 30 mm and diameters 1.6, 1.4, 1.2, 1.0, 0.8 and 0.6 mm reconstructed with the list-mode MLEM method (100 iterations). The voxel size was $0.15 \times 0.15 \times 0.15$ mm^3. No attenuation or scatter corrections were applied. The source activity was low enough that random coincidences could be ignored. Rods of diameter 0.6–1.6 mm are visible.

4. Conclusion

The potential imaging performance of a high-resolution liquid xenon (LXe) preclinical PET system was evaluated with Monte Carlo simulations. An event reconstruction algorithm was developed to handle multiple photon scatterings in LXe, enabling us to refine the LOR selections and reduce the event mispositioning introduced by scattered and random events which result in background noise. Using an energy window [450 600] keV which is possible due to the high energy resolution, the results show that the LXePET system combines uniform high-resolution radial, tangential and axial position measurements throughout the FOV ($\leqslant$0.8 mm FWHM) with high sensitivity (12.6% at CFOV) and the ability to reject scatter and

random coincidences. The scatter fraction was found to be 20.8% (12.1%), with associated peak NECR values of 1326 kcps at 188 MBq (705 kcps at 184 MBq) for mouse(rat)-like phantoms. These results show the potentially excellent imaging capabilities of the LXePET systems. Weighting schemes, where all available data are kept but each LOR is assigned a weight between 0 and 1, and filtering methods based on the test statistic score computed with Compton kinematics will be investigated to further decrease noise in the images. Measurements are in progress to demonstrate the performance of the LXePET system described here.

Acknowledgments

This work was supported in part by NSERC, CIHR (CHRP Program), the Canada Foundation for Innovation, the University of British Columbia and TRIUMF which receives founding via a contribution agreement with the National Research Council of Canada.

References

Agostinelli S *et al* 2003 G4—a simulation toolkit *Nucl. Instrum. Methods* A **506** 250–303

Amaudruz P, Bryman D, Kurchaninov L, Lu P, Marshall C, Martin J P, Muennich A, Retiere F and Sher A 2009 Simultaneous reconstruction of scintillation light and ionization charge produced by 511 keV photons in liquid xenon: potential application to PET *Nucl. Instrum. Methods* A **607** 668–767

Aprile E, Curioni A, Giboni K L, Kobayashi M, Oberlack U G and Zhang S 2008 Compton imaging of MeV gamma-rays with the liquid xenon gamma-ray imaging telescope (LXeGRIT) *Nucl. Instrum. Methods* A **593** 414–25

Aprile E *et al* 2007 Observation of anti-correlation between scintillation and ionization for MeV gamma-rays in liquid xenon *Phys. Rev.* B **76** 014115

Arman R 2005 Statistical list-mode image reconstruction and motion compensation techniques in high-resolution positron emission tomography *PhD Thesis* The University of British Columbia

Bao Q, Newport D, Chen M, Stout D B and Chatziioannou A F 2009 Performance evaluation of the inveon dedicated PET preclinical tomograph based on the NEMA NU-4 standards *J. Nucl. Med.* **50** 401–8

Barrett H H, White T and Parra L C 1997 List-mode likelihood *J. Opt. Soc. Am.* A *Opt. Image Sci. Vis.* 2914–23

Chepel V *et al* 1994 Purification of liquid xenon and impurity monitoring for a PET detector *Nucl. Instrum. Methods* A **349** 500–5

Conti E *et al* 2003 Correlated fluctuations between luminescence and ionization in liquid xenon *Phys. Rev.* B **68** 054201

Hudson M and Larkin R 1994 Accelerated image reconstruction using ordered subsets of projection data *IEEE Trans. Med. Imaging* **13** 601–9

Lamare F, Ledesma Carbayo M J, Cresson T, Kontaxakis G, Santos A, Le Rest C C, Reader A J and Visvikis D 2007 List-mode-based reconstruction for respiratory motion correction in PET using non-rigid body transformations *Phys. Med. Biol.* **52** 5187

Marx J N *et al* 1978 The time projection chamber *Phys. Today* **31** 46

Miceli A *et al* 2011 Liquid xenon detectors for positron emission tomography *J. Phys.: Conf. Ser.* **312** 062006

Moszynski M, Szawlowski M, Kapusta M and Balcerzyk M 2002 Large area avalanche photodiodes in scintillation and *x*-rays detection *Nucl. Instrum. Methods* A **485** 504–21

NEMA Standards Publication 2008 Performance measurements of small animal positron emission tomographs National Electrical Manufacturers Association NU(4), Rosslyn, VA

Oberlack U G *et al* 2000 Compton scattering sequence reconstruction algorithm for the liquid xenon gamma-ray imaging telescope (LXeGRIT) arXiv:astro-ph/0012296

Parra L and Barrett H H 1998 List-mode likelihood: EM algorithm and image quality estimation demonstrated on 2D PET *IEEE Trans. Med. Imag.* **17** 228–35

Pratx G, Surti S and Levin C 2011 Fast list-mode reconstruction for time-of-flight PET using graphics hardware *IEEE Trans. Nucl. Sci.* **58** 105–9

Rahmim A, Cheng J-C, Blinder S, Camborde M-L and Sossi V 2005 Statistical dynamic image reconstruction in state-of-the-art high-resolution PET *Phys. Med. Biol.* **50** 4887

Rahmim A, Ruth T J and Sossi V 2004 Study of a convergent subsetized list-mode EM reconstruction algorithm *Nucl. Sci. Symp. Conf. Record, 2004 IEEE* **6** 3978–82

Reader A J 2004 List-mode EM algorithms for limited precision high-resolution PET image reconstruction *Int. J. Imaging Syst. Technol.* **14** 139–45

Roldan P S *et al* 2007 Raytest ClearPET(TM), a new generation small animal PET scanner *Nucl. Instrum. Methods* A **571** 498–501

Seidel J, Vaquero J J, Pascau J, Desco M, Johnson C A and Green M V 2002 Features of the NIH atlas small animal PET scanner and its use with a coaxial small animal volume CT scanner *Biomed. Imag. Biol.* pp 545–8

Shepp L A and Vardi Y 1982 Maximum Likelihood Reconstruction in Positron Emission Tomography *IEEE Trans. Med. Imaging* **1** 113–22

Tai YC, Ruangma A, Rowland D, Siegel S, Newport D F, Chow P L and Laforest R 2005 Performance evaluation of the microPET focus: a third-generation microPET scanner dedicated to animal imaging *J. Nucl. Med.* **46** 455–63

Yang Y, Wu Y, Qi J, St James S, Du H, Dokhale P A, Shah K S, Farrell R and Cherry S R 2008 A prototype PET scanner with DOI-encoding detectors *J. Nucl. Med.* **49** 1132–40